LASER & PHOTONICS REVIEWS
www.lpr-journal.org

On-Demand Tailoring of Optical Branched Flow via Soft Matter Domain Engineering

Xiao Yu, Xin-Yu Fang, Jing-Qi Tian, Xing-Zhou Tang, Zi-Ye Wang, Jin-Hui Chen, Yan-Qing Lu,* and Bing-Xiang Li**

Soft matter materials, known for their exquisite sensitivity to external stimuli, have facilitated the engineering of intriguing superstructures, driving groundbreaking advancements in photonics devices. However, in-plane manipulation of optical beams remains challenging, especially in the presence of complex scattering phenomena such as branched flow. Here, the controlled design of branched light flow, beginning with fundamental beam refractions in soft nematic liquid crystals (NLCs), is demonstrated. Leveraging a multistep photoalignment technique, disordered optical potentials are generated by exploiting the intricate inhomogeneity of NLC domain mesostructures. By tuning the density of these domains, the correlation length of disordered potential can be adjusted, thereby enabling control over the branched flow of light. The unconventional intensity statistics and the rapid fidelity decay along propagation are revealed through in-plane light scattering, illuminating the complex dynamics of light–matter interactions. Furthermore, a phenomenon that transcends the classical understanding of branched flow is uncovered: the emergence of unilateral branches at the boundary of disordered regions of NLCs. This work underscores the unique capabilities of the customizable soft matter platform in shaping the very nature of light transport in planar disordered media and offers a new approach toward novel soft photonics and diffractive optical computing.

1. Introduction

Branched flow is a captivating phenomenon that emerges when waves propagate through a disordered medium with a correlation length exceeding the wavelength and sufficiently small potential strength.[1] Unlike random speckle patterns, a weakly disordered environment fosters focused filaments that intricately divide, forming tree-like caustic distributions.[2] Although fundamentally linear, branched flow can lead to high field intensities that catalyze nonlinear wave phenomena such as tsunamis,[1a] breathers,[3] and rogue waves.[4] Initially observed in two-dimensional (2D) electron gases,[5] branched flow has been identified in various physical systems, including microwaves,[6] sound waves,[7] and water waves.[8] Recently, the branched flow of light was reported by leveraging the smooth thickness variations of the soap film as a correlated disordered potential.[9] This discovery has aroused research interests in in-plane light field manipulations,[10] given the unconventional intensity distribution arising from branching behavior on both flat and rough curved surfaces,[11] as well as its potential application in optical computing devices.[12] The on-demand design of disordered optical potentials for manipulating and customizing branched flow is highly anticipated for practical photonic applications.

Very recently, some soft matter materials, such as liquid crystals (LCs), have been reported to offer novel opportunities for manipulating the branched flow of light.[10] LCs, as representative soft matter, combine properties of isotropic fluid and crystalline solids possessing properties of dielectric anisotropy and optical birefringence.[13] Early research revealed the responsive behavior of LC molecules to external stimuli such as electric fields,[14] magnetic fields,[15]

X. Yu, X.-Y. Fang, J.-Q. Tian, X.-Z. Tang, Z.-Y. Wang, B.-X. Li
College of Electronic and Optical Engineering & College of Flexible Electronics (Future Technology)
Nanjing University of Posts and Telecommunications
Nanjing 210023, China
E-mail: bxli@njupt.edu.cn

X. Yu, Y.-Q. Lu, B.-X. Li
National Laboratory of Solid State Microstructures
Key Laboratory of Intelligent Optical Sensing and Manipulation
College of Engineering and Applied Sciences
and Collaborative Innovation Center of Advanced Microstructures
Nanjing University
Nanjing 210023, China
E-mail: yqlu@nju.edu.cn

J.-H. Chen
Institute of Electromagnetics and Acoustics
Xiamen University
Xiamen 361005, China
E-mail: jimchen@xmu.edu.cn

J.-H. Chen
Shenzhen Research Institute of Xiamen University
Shenzhen 518000, China

The ORCID identification number(s) for the author(s) of this article can be found under https://doi.org/10.1002/lpor.202401717

DOI: 10.1002/lpor.202401717

optical exposure,[16] and surface anchoring.[16a,17] These findings have enabled the multiple customizations of molecular orientation, offering a tremendous advantage in domain engineering. As an important topic, domain engineering in LCs advanced intriguing superstructures,[18] which have been applied to multitudinous photonics devices including linear and nonlinear light field manipulation,[17b,19] with some demonstrating optical efficiency comparable to traditional crystals.[19c] Typically, the elementary units of LC devices are fabricated as sandwich-like structures, naturally functioning as waveguides for planar wave propagation.[20] Notably, topological beam steering through designed LC vortices has been reported, analogous to the cosmic strings.[21] Given their extreme sensitivity to external stimuli, LCs have been investigated as dynamic platforms for studying electrical switching[10a] and the transition of optical branched flow.[10b] Previous studies have primarily focused on macroscopic control of optical branching. However, in these works, disordered potentials arise spontaneously due to the self-assembly patterns of LC films. Consequently, the branched flow fields cannot be tailored on demand, highlighting the need for an approach that enables precise customization of disordered optical landscapes.

In this work, we present an experimental realization of customizing optically disordered potentials through domain engineering within soft NLC. This strategy facilitates the manipulation of in-plane beam deflection and the tailoring design of the branched flow of light. By using the photoalignment technique to orient NLC molecules, we create optical domains with specific refractive indices, resulting in in-plane beam deflections that approximately adhere to classical Snell's law. By assembling these domains with varying densities, multiple disordered potentials characterized by extended correlation lengths are created, enabling the controlled formation of the branched flow of light in the desired position within a homogenous environment. Moreover, the presence of the boundary of disordered soft matter leads to the emergence of unilateral branches, extending the conventional understanding of branched flow.

2. Results and Discussion

2.1. Experimental Setup

We present an experimental setup, as illustrated in **Figure 1a**, designed for the on-demand creation of branched flow of light in a planar LC-based soft matter system. The optical devices are fabricated into a sandwich-like structure, composed of two glass substrates, each spin-coated with a polarization-sensitive alignment layer of optically sulfonic azo-dye (SD1), as shown in Figure 1b. The two substrates are glued with a gap $d \approx 35$ μm. Subsequently, the cell undergoes ultraviolet (UV) light treatment with multistep exposure, including uniform-polarized UV light (Figure 1c) and a digital micromirror device (DMD)-based microlithography system, empowering on-demand customization of LC textures in a homogeneous background (Figure 1d and Experimental Section). After alignment, the NLC material E7, which possesses positive permittivity anisotropic, $\Delta\varepsilon = \varepsilon_{//} - \varepsilon_{\perp} > 0$ is infiltrated into the cells, forming a soft membrane that facilitates in-plane optical wave propagation. In the NLCs, which are uniaxial materials with long-range orientational order, the director $\hat{\mathbf{n}}$ represents both the average orientation of molecules and the optical axis.[22] Due to the isomerization and dichroic absorption of the azo-dye layers, SD1 molecules tend to reorient perpendicular to the polarization of the UV light, which, in turn, aligns adjacent LC molecules, thus guiding the director $\hat{\mathbf{n}}$.[20] Using a polarized optical microscope (POM), we can observe the LC textures under different exposing conditions, as shown in Figure 1e,f. The background nematic is uniformly aligned along the x-axis, marked as $\hat{\mathbf{n}}_0 = (1, 0, 0)$(Figure 1g). To induce refractive index variations and create a disordered potential, the director of NLC within the specific pattern is deflected relative to the background alignment, as exemplified $\hat{\mathbf{n}}_i = (0, 1, 0)$ in Figure 1h. We investigate the manipulation of in-plane beam propagation and the formation of feasible caustics using these textures with linearly polarized light incidence, where the beam's polarization direction is parallel to the y-axis (Figure S1, Supporting Information). The sandwich-like structure of the LC sample serves as a waveguide, confining the optical beam along the longitudinal direction (z-axis). The Gaussian beam is focused at the sample entrance, with a beam waist of $w_0 \approx 20$ μm, and the Rayleigh length is calculated to be ≈2 mm. Due to the high optical losses in the NLC medium, the beam propagation is significantly attenuated before reaching the Rayleigh length. Using the optical microscope (Figure S2, Supporting Information), the optical field propagating through the NLC membrane can be captured due to Rayleigh scattering.[22] Weakly scattered beam propagation was observed in the homogeneous state (Figure 1i), whereas designed branched flows emerged within a correlated disordered potential (Figure 1j), which will be discussed in more detail later.

2.2. In-Plane Beam Deflection Based on Local NLC Domain Engineering

Domain engineering with a specific refractive index is a fundamental research topic in optical transition control, enabling phenomena such as wide-angle deflection and optical caustics.[23] We present experimental results on beam deflection through the design of NLC domains with director mutation, as illustrated in **Figure 2a**. Due to optical birefringence, a uniform NLC system can propagate light with two distinct polarizations: one perpendicular to the LC plane, known as an ordinary wave (o-wave), and the other parallel to the plane, known as an extraordinary wave (e-wave). As previously mentioned, the polarization of the incident beam is aligned along the y-axis, corresponding to an e-wave due to the homogeneous orientation of the LC director within the x–y plane. In the experiment, the enclosed NLC layer within the sandwich-like cell structures forms a waveguide that enables the propagation of optical waves, with the e-wave propagation following the Helmholtz equation[9a]

$$-\nabla_{xy}^2 \psi + V(x, y)\,\psi = k_0^2 \bar{n}^2 \psi \tag{1}$$

here ψ represents the field amplitude of the optical field component of e-wave, k_0 is the value of wavevector in vacuum. In the experiment, the wavevector direction is set along the x-axis, and the operator executes $\nabla_{xy}^2 = \partial^2/\partial x^2 + \partial^2/\partial y^2$; for the optical wave,

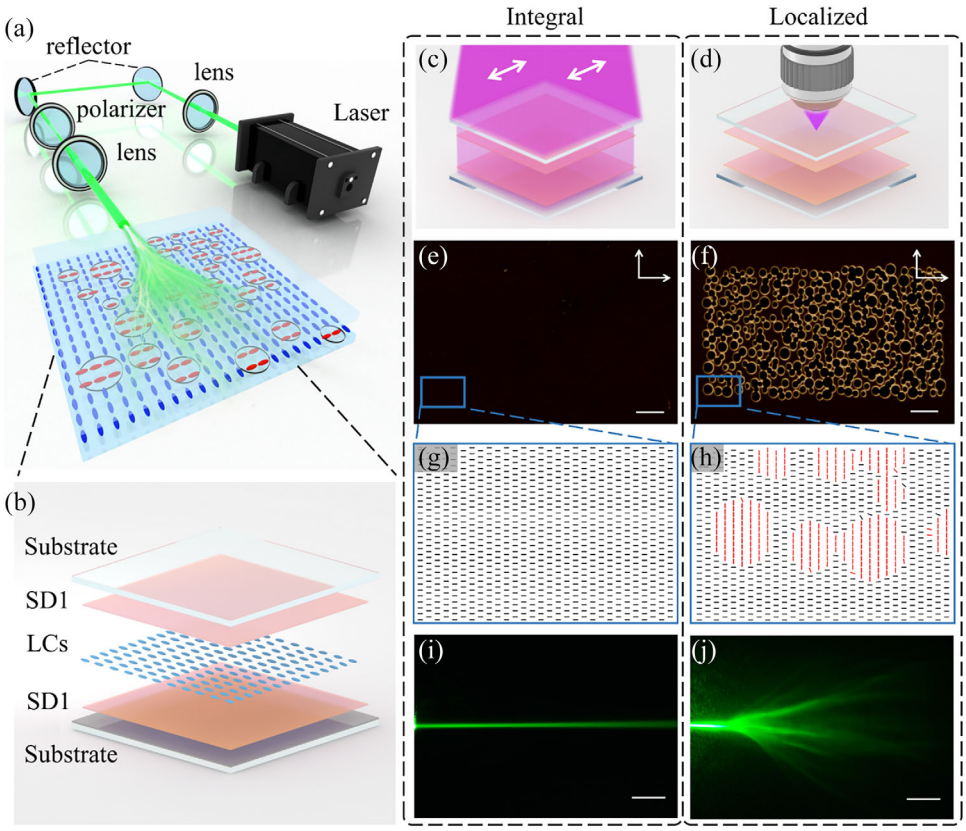

Figure 1. Branched flow of light in domain-engineered NLCs. a) Experimental setup to observe the branched flow of light in NLC film. b) Schematic diagram of the NLC cell. The orange layers represent the photo-sensitive alignment layers (SD1), and the blue rods illustrate the NLC directors. Schematics demonstrate multistep exposure including c) integral orientation and d) localized pattering of the NLC directors. The inset white arrows represent the polarization of UV light. POM diagrams of the NLC textures: e) uniform alignment structure and f) disordered NLC domain distributions. g,h) Director orientation of the local NLC textures extracted within the rectangles marked in (e) and (f). Microscope images showcasing the propagating behavior of the optical beams in NLC film: i) weak scattering state in the homogeneous NLC layer and j) optical branched field traversing the designed disordered-domain NLC film. All scale bars represent 200 µm.

$k_0^2\bar{n}^2$ plays the role of the total energy ($E_{tot} = k_0^2\bar{n}^2$) with potential $V(x, y)$ forming by $V(x, y) = k_0^2(\bar{n}^2 - n_{eff}^2(x, y))$. $n_{eff}(x, y)$ is the locally effective refractive index of the e-wave and $\bar{n} = \langle n_{eff}^2 \rangle$ is obtained by averaging the refractive index of the whole landscapes.

Figure 2a demonstrates rounded domains (RDs) with different designs of the inner director ($\widehat{\mathbf{n}}_i$), which might lead to a wall defect[22] as observed under the POM (Figure S3, Supporting Information). The formation of these defects due to the self-assembled LC molecules occurs naturally in the transition region between two domains, especially at large mutations of the director (Figure S3, Supporting Information).[24] We coupled the polarized Gaussian beam at various locations along the interface between two LC domains and observed the resulting beam deflection with the microscope, as shown in Figure 2b and Figure S4 (Supporting Information). To better observe the integral beam refraction, a quasi-plane wave incidence using a cylindrical lens was employed (Figure S1b, Supporting Information). The beam deflection within the RDs intensifies with the orientational angle of the internal director (φ_i), resulting in a high-intensity focus as the plane wave passes through the domain (Figure 2c). Figure 2d illustrates the beam deflection geometry. In the homogeneously treated background ($\varphi = 0°$), the refractive index for the incident beam is denoted by $n_0 = n_\perp$ (n_o). Under these conditions, birefringence does not occur. In contrast, when the beam reaches the interface of the LC domains, the nonzero angle between the wave vector (k) and the inner director ($\widehat{\mathbf{n}}$) determines the degree of refractive index $n_i = n_{eff}(\varphi)$, further allowing for the beam deflections

$$n_{eff}(x, y) = \frac{n_\perp n_{//}}{\sqrt{n_\perp^2(1 - \sin^2\alpha\cos^2\varphi) + n_{//}^2\sin^2\alpha\cos^2\varphi}} \quad (2)$$

where α and φ represent the polar angle and the azimuthal angle of the director, respectively (as shown in the inset diagram of Figure 2e); and $n_\perp$ and $n_{//}$ are the refractive indices perpendicular (ordinary refractive index) and parallel (extraordinary refractive index) to the director, respectively. For the complanate (x–y plane) arrangement of the LC director, the polar angle is absent ($\alpha = 90°$), and the in-plane rotation of the director is recorded by φ leading to variations in the effective index, as shown in Figure 2e.

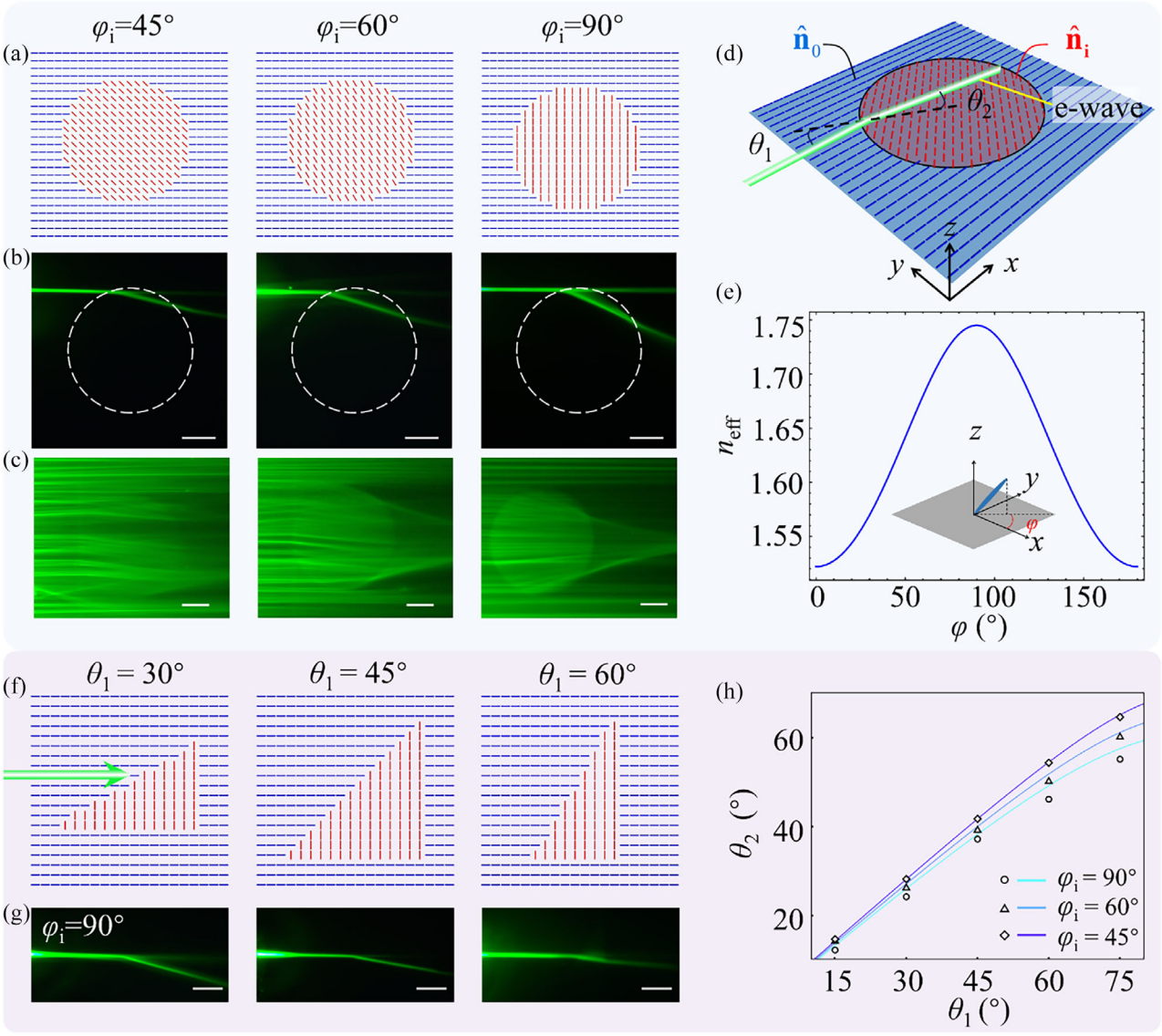

Figure 2. In-plane light beam deflection based on the NLC domain engineering. a) Schematic director map of the rounded NLC domains with different inner director distributions: 45°, 60°, and 90°. The blue sticks represent the director distributions in the background ($\varphi_i = 0°$), and the red sticks represent the inner director orientation. b) Corresponding beam deflections with Gauss beam incidence at the top of the LC domains. The dotted line represents the edges of the RDs. c) Micro images depict the whole distribution of incident board beam after deflection by different domains. d) Perspective diagram illustrates the beam propagation in a homogeneous background and deflection after interacting with the defect walls. θ_1 and θ_2 represent the angle of incidence and deflection, respectively. e) Effective refractive index as a function of the azimuthal angle of the director (φ). The insect diagram demonstrates the azimuthal (φ) and polar angle (α) of the director. f) Schematic director map of the triangular NLC domains with different slopes but an identical inner director distribution ($\varphi_i = 90°$). g) Micro images illustrate the phenomenon of correlated beam deflection when a Gauss beam makes contact with the hypotenuse at varying incident angles: $\theta_1 = 30°$, $\theta_1 = 45°$, and $\theta_1 = 60°$, respectively. h) Comparative analysis of Snell's law and the experimental beam refraction when impacting the domain walls with different incident angles. The colored curves represent the theoretical value of the law and the black spots with different shapes represent the experimental data. The scale bar is 200 µm.

In addition, although the circular geometry appears straightforward, it permits varying angles of incidence ($0° < \theta_1 < 90°$) when parallel beams strike it at different points, as illustrated in Figure 2d. To observe the refractive behaviors at different incident angles, we designed triangular domain structures and kept the incident beam horizontally in contact with the hypotenuse, as shown in Figure 2f and Figure S5 (Supporting Information). Figure 2g shows an example of the controlled experiment where the inner director is set along the *y*-axis ($\hat{\mathbf{n}}_i = (0, 1, 0)$) and demonstrates that the degree of beam reflection increases with the angle of incidence. We conclude Snell's law from comprehensive beam deflection with various incidence angles (θ_1) and effective index of refractive ($n_{eff}(\varphi)$)

$$n_0 \sin\theta_i = n_i(\varphi) \sin\theta_2 \tag{3}$$

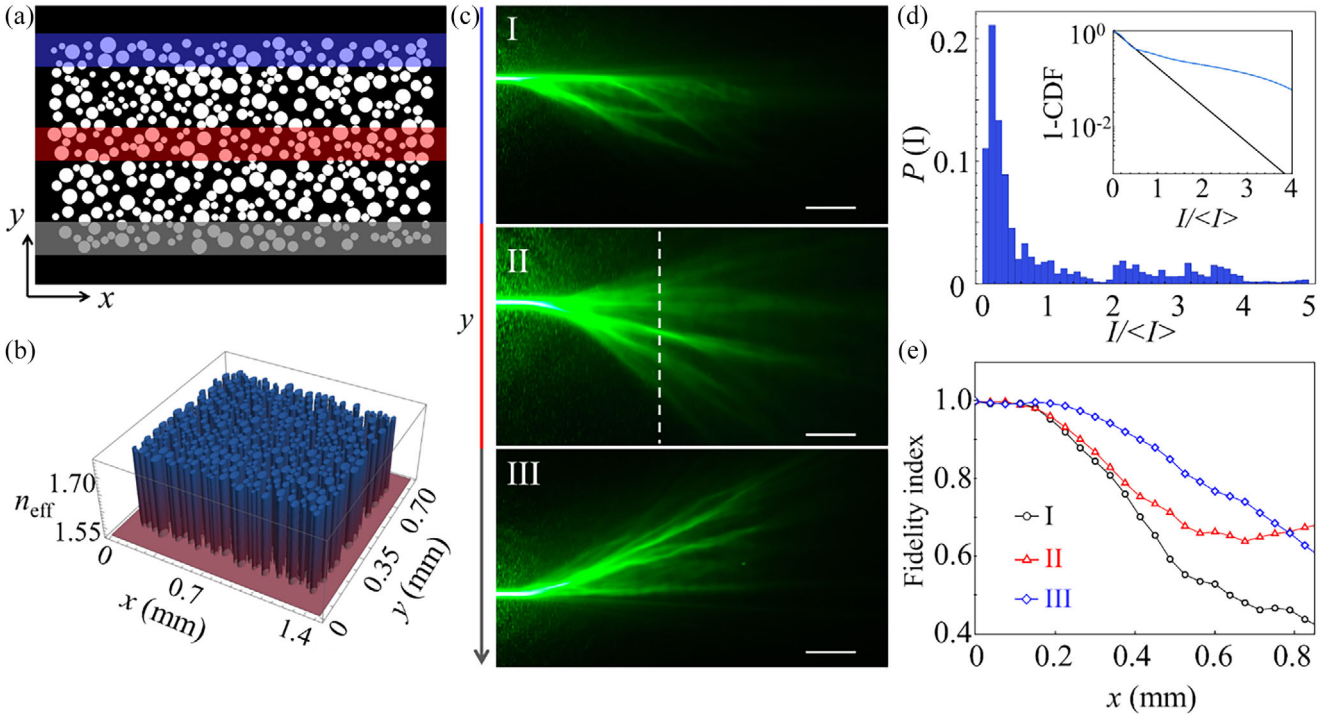

Figure 3. Tailoring branched flow of light in homogeneous NLC backgrounds. a) Examples of binary diagrams depict blueprints of disordered patterns containing 400 RDs. The black areas represent a homogeneous NLC background, while the white spots indicate the distribution of mutated regions. b) A schematic diagram illustrates the effective refractive index of the customized disordered pattern. c) The top-viewed branched flow of light observed when the Gauss beam passes through the top region (I), intermediate region (II), and bottom region (III) of the patterns. Corresponding incident positions are indicated by different colored rectangles marked in (a). d) The probability distribution of optical branched fields. The intensity data of the branched flow is extracted from the linear channel, as marked in (c). e) Optical fidelity index as a function of beam propagation distance. Scale bar 200 μm.

where θ_1 and θ_2 represent the angle of incidence and refraction, respectively. n_0 and $n_i(\varphi)$ are the refractive indexes of two domains on either side of the defect walls, respectively. The colored-distinguished curves shown in Figure 2h demonstrate the theoretical values of the refraction angle as a function of the incidence angle. The experimental results, represented by differently shaped markers in Figure 2h, generally agree well with the theoretical curves. However, it is important to note that the experimental values are slightly lower than the theoretical predictions, especially when $\varphi_i = 90°$. This discrepancy may be attributed to the continuous rotation of the director at the boundary of the exposure area, resulting in a reduction of the actual effective index.

2.3. On-Demand Tailoring of Weakly Disordered Landscapes Capable of Forming Optical Branched Fields

Correlated disordered media have been widely studied for their impact on wave propagation, including optical localization, diffusion, and scattering optimization.[25] Branched flow, a complex scattering phenomenon, arises when waves encounter a weakly disordered potential landscape. In this work, we generate such disordered potentials by utilizing the spatial distribution of RDs, as shown in **Figure** 3a. These patterns are formed by randomly assembling RDs without overlap, enabling strong beam deflections that ultimately lead to a branched flow of light. In our experiments, we controlled the number of RDs within a given area, while removing the constraints on their size and configuration, provided that mutual occlusion was avoided. This method enables the generation of a large variety of patterns with similar density of director mutation areas, as shown in Figure S6 (Supporting Information). More importantly, the random barycenter and size distribution of these domains within a fixed area forms weakly disordered potentials, despite using only two different director orientations, distinguishing this approach from previous studies.[10] To enhance visualization, we analyzed the correlation properties (Figure S7, Supporting Information), demonstrating a direct relationship between correlation characteristics and domain density.

The statistical properties of the wave field in the branched flow are determined primarily by the correlation length l_c and the relative strength of the disordered potentials ϵ rather than by the other specific features.[9a] To verify this dependency in our model, we first compare the branching landscapes generated by disordered patterns with different correlation properties while maintaining the filling fraction (Figure S8, Supporting Information). The results show that the strength of the correlated potentials can be modulated by altering the effective refractive index without changing the domain distribution. More importantly, the transition of the branched fields indicates that the branched flow in our model is linked to the correlation properties of the disordered structures. To enhance the ability of LC domains to form caustics and ultimately facilitate branched flow, we selected RDs with an inner director orientation perpendicular to the background

for constructing the disordered landscapes used in subsequent studies. Figure 3b depicts the landscape morphology in terms of effective refractive index, which directly promotes the in-plane optical behaviors, including beam steering and optical branched flow,[9a,10] as shown in Figure 3c. However, it is important to note that the optical potential varies with the injection direction of the optical wave due to the birefringence of the NLC membrane and the binary design strategy, as shown in Figure S9 (Supporting Information).

For the NLC film photopatterned using the model, the calculated correlation length l_c is on the scale of 50 μm, and ϵ is ≈0.06, satisfying the basic requirements for branched flow. Figure 3c illustrates the observation of branched flow of light with varying geometrical characteristics. The classical scenario of optical branched flow exists in the intermediate area (II) of the patterns when a Gauss beam is coupled (middle panel in Figure 3c). By precisely adjusting the incident position of the optical beam passing through the LC pattern, unilateral flow of branched fields can also be obtained at the top (I) and bottom (III) regions of the LC patterns (Figure 3c top and bottom panels), attributed to the boundary asymmetry of the disordered landscape. One important characteristic of the branched flow is its unconventional distribution of intensity, which is typically analyzed by measuring its probability density. Figure 3d shows the probability distribution of the intensity data extracted from the linear cross-section, as indicated in Figure 3c. The cumulative distribution function (CDF) of the branched flow is shown in the inset diagram, highlighting the important characteristic that, the CDF deviates from the Rayleigh distribution at high intensities. This deviation is linked to the development of high-intensity filaments.[9a,10a,11c] To further analyze the scattering properties of each branched field during movement, we introduce the fidelity index, which captures the transformation of the beam along its propagation path (Note SI, Supporting Information).[10] In the definition, the fidelity $F(x)$ mathematically characterizes the deformation of the optical field as it propagates along the x-direction. A high-fidelity value indicates that the optical field retains its shape and structure during propagation, whereas low fidelity suggests significant deformation due to light scattering effects in disordered media. Notably, the fidelity index of the branched fields degrades rapidly over a propagation distance of about 0.2 mm, which is consistent with the first branch position.[10a,11a] The single measurement of fidelity shows the varying dynamics of propagating branched fields, which are determined by the local disordered potential (Figure 3e).

We further investigate the asymmetric flow at the interface between ordered and disordered structures, ensuring that both regions have the same filling fraction, as shown in Figure S10 (Supporting Information). When the optical beam propagates along this interface, the branched flows predominantly extend into the disordered potential field, maintaining their unilateral propagation (Figure S10, Supporting Information). In addition, as the disc region possesses a higher refractive index than the background, part of the beam propagates as straight leaky-wave-like rays toward the ordered region without forming branches. These observations highlight the critical role of weakly disordered potential fields in generating branched flow, while the overall beam trajectory remains governed by the effective refractive index.

Following the principle of organizing disordered landscapes, we can create patterns with alternative densities of RDs, as shown in **Figures** 4a and S11 (Supporting Information). The top-view images of the branched fields are observed (Figure 4b,c and Figures S12–S16, Supporting Information). For the branched flow generated by an incident Gaussian beam, both the branching strength and the flowing width decrease as the domain density increases. This trend is evident in the intensity distribution across the cross-section (Figure 4d). Although the general correlation length of the potential landscape decreases with increasing domain density (Figure S7, Supporting Information), the local landscapes interacting with the Gaussian beam (width of 30 μm) become more ordered due to the connectivity between adjacent domains. As a result, the fidelity index exhibits a more gradual decline as the domain density increases (Figure 4e). In the case of quasi-plane wave incidence, the wave focuses at a specific distance (first branching distance), which varies between different disordered potential landscapes, as seen in Figure 4c. The scintillation index provides a direct way to extract the branching distance from experimental data[26] (Note SI, Supporting Information). To quantify intensity fluctuations, we measure the intensity over the transverse coordinate by averaging across different branching realizations from potentials with the same correlation properties (l_c, ∈), as shown in Figure 4f and Figure S17 (Supporting Information). This averaging dataset characterizes the statistical variations in optical wave intensity as it propagates through the disordered medium. Figure 4f shows the extracted scintillation index of the propagating optical fields around the peak positions for different densities. Using the ensemble averaging method, the first branching distance d_f of each branched field can be extracted from the peak position of the average scintillation index curve. These peak positions were measured as ≈301 μm (N = 400), 270 μm (N = 450), 262 μm (N = 500), 253 μm (N = 550), and 234 μm (N = 600), as shown in Figure S17f (Supporting Information). Due to the limited number of experimental samples, the relative deviations of the experimental results from the theoretical predictions are ≈1.8%. Intriguingly, the shift of the peak position directly observed in the scintillation index, demonstrates the advantage of customizing disordered potential fields compared to previous work.[9a,10,27]

To obtain the branching distance theoretically, we analyze the potential environment of these disordered landscapes. As already mentioned, the correlation length (l_c) and potential strength (∈) are important statistical characteristics of the randomly disordered potential and help determine the theoretical properties of the branched flow, including the branching distance. The correlation length and potential strength are defined by a correlation function, written as $c(r) = \langle V(r)V(0)\rangle = \sigma^2 f(\vec{r}\cdot\vec{r}/l_c^2)$, with potential $\in = \sigma/2E_{tot} = \sqrt{V^2}/2k_0^2\bar{n}^2$ and $f(0) = 1$.[9a] The correlated function can take various forms, typically including the exponential decay function and Gaussian function. In our analysis, the strength and length of the correlated potential are calculated by measuring the width of the autocorrelation function corresponding to the refractive index landscape (Figure 4g and Figure S7, Supporting Information). As expected, the correlation of the optical potential decreases with the density of the RDs, while the potential strength remains around a constant ∈= 0.06 (Figure 4g). The first branching distance can be

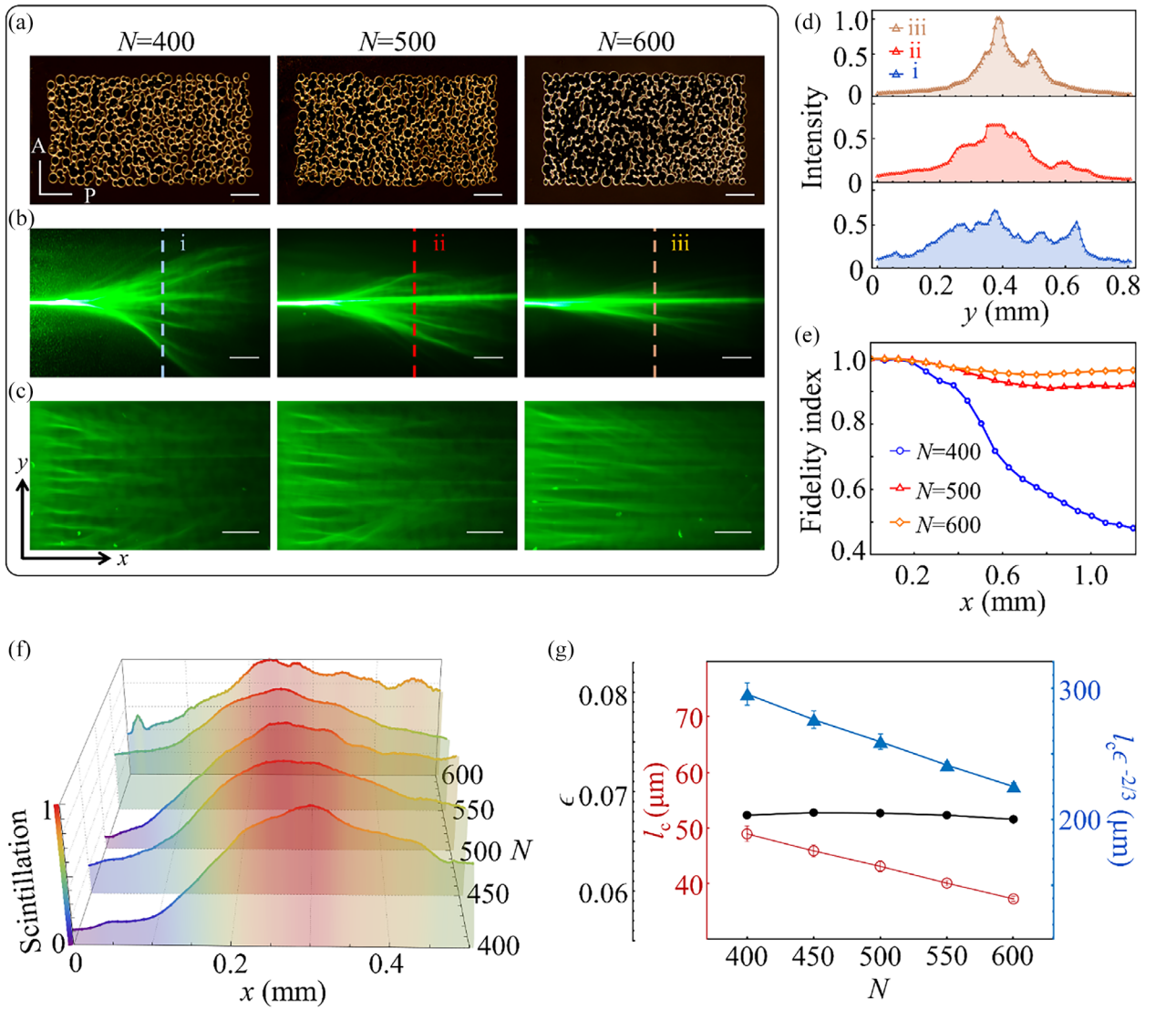

Figure 4. Tuning branched flow of light through regulatory domains engineering. a) POM diagrams of customized disordered patterns with different numbers of RDs, respectively, N = 400, 500, 600. The scale bar is 200 μm. Microscope images of optical branched flow in corresponding optical landscapes, with b) Gauss beam and c) quasi-plane wave incidence. The scale bar is 200 μm. d) Cross-section optical intensity of branched field in different potentials. The intensity data was extracted from the linear cross position marked in (b). e) Fidelity index as a function of propagating distance (x-axis) for each branched field. f) Averaged scintillation index as a function of the propagation distance x, extracted from the plane-wave experiments conducted with different numbers of LC domains (N = 400, N = 450, N = 500, N = 550, N = 600). g) Correlation length (l_c), potential strength (ϵ), and theoretical first branching distance ($l_c\epsilon^{-2/3}$) as a function of the number of randomly distributed domains.

calculated based on the statistical length scale of $d_f \propto l_c\epsilon^{-2/3}$, as shown in Figure 4g, which agrees well with the experiments. In addition, modifying the packing arrangement of these circular domains while maintaining a constant filling fraction also enables disordered photonic structures to exhibit different degrees of order,[25b] leading to different spatial correlation and corresponding transformations of branched fields (Figure S18, Supporting Information). This supplementary analysis further confirms that the branched flow in our model is not solely dictated by the density of the discs but is intrinsically governed by the correlation properties of the disordered potentials.

3. Conclusion

In this study, we have experimentally realized the in-plane control of an optical beam, from its fundamental deflection to the on-demand design of branched flow of light in the NLC medium. Utilizing the photoalignment technique, we are able to design the local orientation of the NLC director, enabling the creation of optical domains with specific refractive indices. We demonstrated the optical reflection behavior through the design of these LC domains and subsequently validated Snell's law. By assembling these LC domains with a higher refractive index into a fixed area, we produced multiple optical potentials with alternative

disordered states, thereby enabling the generation of a branched flow of light at desired locations within a homogeneous environment. This novel method, utilizing only two distinct director orientations, enables precise tailoring of disordered potential fields through the spatial distribution of domains. Furthermore, by fully leveraging the liquid crystal orientation and independently designing the director configuration between domains, the dependence of optical branched flow on the incident direction could be eliminated. This strategy not only enhances the universality of branched flow control but also broadens its applicability to other physical systems. We envision that wide-angle deflection, such as the U-turn of an optical beam, can be realized in an NLC membrane through material engineering,[28] precise alignment, and polymerization techniques.[20,23] Overall, this research demonstrates that a soft matter system, facilitated by the alignment technique, can serve as an excellent platform for controlling planar beam transmission—from simple deflection to complex scattering—and paves the way for novel optical computing devices.

4. Experimental Section

Materials: The NLC material E7 (Jiangsu Hecheng Display Technology) was used for the fabrication of the LC-based waveguide. E7 undergoes a phase transition from isotropic to nematic at 60.5 °C and exhibits refractive indices of 1.74 for the e-wave (n_e = 1.74) and 1.52 for the o-wave (n_o = 1.52) at room temperature (25 °C). The material's dielectric anisotropy was measured and characterized.

Sample Fabrication: The indium tin oxide (ITO)-coated glass substrates were first cleaned in an ultrasonic bath with deionized water at 50 °C for 20 min to remove surface impurities. Following this, the substrates were subjected to UV–ozone treatment at 50 °C for 30 min to eliminate any remaining organic contaminants, thereby promoting uniform deposition of the alignment layer. The alignment layer, consisting of SD1 dissolved in dimethylformamide (DMF) at a concentration of 0.5 wt%, was spin-coated onto the substrates using a multistep rotation process: an initial spin at 800 rpm for 10 s followed by a secondary spin at 3000 rpm for 30 s. After curing at 100 °C for 10 min, the substrates were assembled into an LC cell using UV-curable glue blended with spacers to achieve a cell thickness of ≈35 µm, as determined by the spacer size.

The Photopatterning of Disordered Potential Landscapes in Uniform NLC: The homogeneous alignment of the LC background was achieved by exposure to a uniformly polarized UV light at a wavelength of 405 nm. During UV exposure, the SD1 molecules align with their long axis perpendicular to the polarization direction of the light source, thereby inducing the orientation of the LC director. For the design of the localized domain, a DMD-based lithography device (Nanjing Ningcui Optical Technology Co., Ltd.) was used for secondary exposure of the LC cell. The DMD, synchronized with an array of rotational motors, provides precise control over polarization direction according to the photopatterning information. Initially, predesigned binary patterns were loaded onto the DMD chip, after which the UV source carried the pattern information, projecting it onto the glass substrates through a high-resolution objective lens. The LC cells were placed on a three-axis (X, Y, Z) motorized stage to precisely control the exposure position. Following the photolithography process, the NLC materials were filled into the LC cell in its isotropic state (at 70 °C) through capillarity.

Optical Setup and Beam Coupling: A continuous-wave laser with a wavelength of 532 nm (Changchun Letime Technology Co., Ltd.) was used and coupled into the LC samples after the adjustments of the beam waist, polarization, and power (Figure S1, Supporting Information). The beam waist was kept smaller than the cell gap, which was controlled by using an optical system consisting of two plano-convex lenses (JCOPTIX, China). The polarization of the incident beam was managed using two polarizers and a wave plate with a quarter wavelength retardation (Figure S1, Supporting Information). The beam passes through the first polarizer, emerging as linearly polarized light, then is converted to circular polarization via the quarter-wave plate, and finally reoriented to linearly polarized light with an adjustable direction, without any intensity difference, by the second polarizer. An attenuator was used to regulate the light's intensity.

Observation of NLC Textures and In-Plane Optical Field: To observe both the LC textures and the correlated optical beam trajectory within the LC layer, a polarized optical microscope was constructed (Figure S2, Supporting Information). The LC textures were observed in a cross-polarized state using an LED light source. The beam trajectory was captured by imaging the optical scattering from a top-view perspective. To accurately measure the intensity distribution of the branched flow, the LED source and polarizers were removed to prevent the loss of optical information.

Supporting Information

Supporting Information is available from the Wiley Online Library or from the author.

Acknowledgements

This work was supported by the National Key Research and Development Program of China (Nos. 2022YFA1405000 and 2023YFA1407104), the National Natural Science Foundation of China (Nos. 62375141 and 12274357), the Natural Science Foundation of Jiangsu Province, Major Project (No. BK20243067), Fujian Provincial Natural Science Foundation of China (No. 2023J06011), Fundamental Research Funds for the Central Universities (No. 20720210045), and Shenzhen Science and Technology Program (No. JCYJ20240813145614019). J.-H.C. also thanks the support of Xiaomi Young Talents Program/Xiaomi Foundation.

Conflict of Interest

The authors declare no conflict of interest.

Author Contributions

X.Y. and X.-Y.F. contributed equally to this work. X.Y. and X.-Y.F. established the experimental devices, fabricated the samples, and performed the experiments with the help of J.-Q.T.; X.Y. built the theoretical model and analyzed the results with the help of J.-H.C., B.-X.L., X.-Z.T., and Z.-Y.W.; B.-X.L. co-supervised the project with J.-H.C. and Y.-Q.L. All authors contributed to the discussion, analyzed the data, and wrote the manuscript.

Data Availability Statement

The data that support the findings of this study are available in the supplementary material of this article.

Keywords

beam control, branched flow of light, domain engineering, liquid crystals, soft matter photonics

Received: October 13, 2024
Revised: March 15, 2025
Published online:

[1] a) E. J. Heller, R. Fleischmann, T. Kramer, *Phys. Today* **2021**, *74*, 44; b) J. J. Metzger, R. Fleischmann, T. Geisel, *Phys. Rev. Lett.* **2010**, *105*, 020601; c) L. Kaplan, *Phys. Rev. Lett.* **2002**, *89*, 184103.
[2] Y. A. Kravtsov, Y. I. Orlov, *Caustics, Catastrophes and Wave Fields*, Springer, Berlin **1993**.
[3] J. M. Dudley, F. Dias, M. Erkintalo, G. Genty, *Nat. Photonics* **2014**, *8*, 755.
[4] L. H. Ying, Z. Zhuang, E. J. Heller, L. Kaplan, *Nonlinearity* **2011**, *24*, R67.
[5] M. A. Topinka, B. J. LeRoy, R. M. Westervelt, S. E. J. Shaw, R. Fleischmann, E. J. Heller, K. D. Maranowski, A. C. Gossard, *Nature* **2001**, *410*, 183.
[6] R. Höhmann, U. Kuhl, H. J. Stöckmann, L. Kaplan, E. J. Heller, *Phys. Rev. Lett.* **2010**, *104*, 093901.
[7] M. A. Wolfson, S. Tomsovic, *J. Acoust. Soc. Am.* **2001**, *109*, 2693.
[8] H. Degueldre, J. J. Metzger, T. Geisel, R. Fleischmann, *Nat. Phys.* **2016**, *12*, 259.
[9] a) A. Patsyk, U. Sivan, M. Segev, M. A. Bandres, *Nature* **2020**, *583*, 60; b) A. Patsyk, Y. Sharabi, U. Sivan, M. Segev, *Phys. Rev. X* **2022**, *12*, 021007.
[10] a) S.-S. Chang, K.-H. Wu, S.-J. Liu, Z.-K. Lin, J.-B. Wu, S.-J. Ge, L.-J. Chen, P. Chen, W. Hu, Y. Xu, H. Chen, D. He, D.-Q. Yang, J.-H. Jiang, Y.-Q. Lu, J.-H. Chen, *Nat. Commun.* **2024**, *15*, 197; b) X. Yu, S.-S. Chang, Z.-Y. Wang, J. Liu, X.-Z. Tang, J.-H. Chen, B.-X. Li, Y.-Q. Lu, *Laser Photonics Rev.* **2024**, *18*, 2400366.
[11] a) H. Degueldre, J. J. Metzger, E. Schultheis, R. Fleischmann, *Phys. Rev. Lett.* **2017**, *118*, 024301; b) S. Barkhofen, J. J. Metzger, R. Fleischmann, U. Kuhl, H. J. Stöckmann, *Phys. Rev. Lett.* **2013**, *111*, 183902; c) J. J. Metzger, R. Fleischmann, T. Geisel, *Phys. Rev. Lett.* **2014**, *112*, 203903; d) W. Ding, Z. Wang, C. Yang, *Photonics Res.* **2023**, *11*, 1992.
[12] T. Yan, R. Yang, Z. Zheng, X. Lin, H. Xiong, Q. Dai, *Sci. Adv.* **2022**, *8*, abn7630.
[13] a) P. G. D. Gennes, J. Prost, *The Physics of Liquid Crystals*, Oxford University Press, Oxford **1993**; b) M. Kleman, O. D. Lavrentovich, J. Friedel, *Soft Matter Physics: An Introduction*, Springer, New York **2002**.
[14] a) B.-X. Li, V. Borshch, R.-L. Xiao, S. Paladugu, T. Turiv, S. V. Shiyanovskii, O. D. Lavrentovich, *Nat. Commun.* **2018**, *9*, 2912; b) B. Senyuk, Q. Liu, S. He, R. D. Kamien, R. B. Kusner, T. C. Lubensky, I. I. Smalyukh, *Nature* **2013**, *493*, 200; c) L.-L. Ma, C.-Y. Li, J.-T. Pan, Y.-E. Ji, C. Jiang, R. Zheng, Z.-Y. Wang, Y. Wang, B.-X. Li, Y.-Q. Lu, *Light: Sci. Appl.* **2022**, *11*, 270.
[15] P. Pincus, *J. Appl. Phys.* **1970**, *41*, 974.
[16] a) H. K. Bisoyi, Q. Li, *Chem. Rev.* **2016**, *116*, 15089; b) Z. Zheng, H. Hu, Z. Zhang, B. Liu, M. Li, D.-H. Qu, H. Tian, W.-H. Zhu, B. L. Feringa, *Nat. Photonics* **2022**, *16*, 226; c) Z.-G. Zheng, Y. Li, H. K. Bisoyi, L. Wang, T. J. Bunning, Q. Li, *Nature* **2016**, *531*, 352.
[17] a) C. Peng, T. Turiv, Y. Guo, Q.-H. Wei, O. D. Lavrentovich, *Science* **2016**, *354*, 882; b) P. Chen, B.-Y. Wei, W. Hu, Y.-Q. Lu, *Adv. Mater.* **2020**, *32*, 1903665; c) Y. Guo, M. Jiang, C. Peng, K. Sun, O. Yaroshchuk, O. Lavrentovich, Q.-H. Wei, *Adv. Mater.* **2016**, *28*, 2353.
[18] W. Hu, P. Chen, Y.-Q. Lu, *Photoactive Functional Soft Materials*, Wiley, Germany **2019**.
[19] a) S.-J. Liu, L. Zhu, Y.-H. Zhang, W. Chen, D. Zhu, P. Chen, Y.-Q. Lu, *Adv. Mater.* **2023**, *35*, 2301714; b) P. Chen, Z.-X. Shen, C.-T. Xu, Y.-H. Zhang, S.-J. Ge, L.-L. Ma, W. Hu, Y.-Q. Lu, *Laser Photonics Rev.* **2022**, *16*, 2200011; c) V. Sultanov, A. Kavčič, E. Kokkinakis, N. Sebastián, M. V. Chekhova, M. Humar, *Nature* **2024**, *631*, 294.
[20] T. Wei, P. Chen, M.-J. Tang, G.-X. Wu, Z.-X. Chen, Z.-X. Shen, S.-J. Ge, F. Xu, W. Hu, Y.-Q. Lu, *Adv. Opt. Mater.* **2020**, *8*, 1902033.
[21] C. Meng, J.-S. Wu, I. I. Smalyukh, *Nat. Mater.* **2023**, *22*, 64.
[22] D.-K. W. Yang, *Fundamentals of Liquid Crystal Devices*, Wiley, Hoboken, NJ **2014**.
[23] M. Mattheakis, G. P. Tsironis, in *Quodons in Mica: Nonlinear Localized Travelling Excitations in Crystals* (Eds: J. F. R. Archilla, N. Jiménez, V. J. Sánchez-Morcillo, L. M. García-Raffi), Springer International Publishing, Cham **2015**.
[24] T. Ouchi, K. Imamura, K. Sunami, H. Yoshida, M. Ozaki, *Phys. Rev. Lett.* **2019**, *123*, 097801.
[25] a) L. Pattelli, A. Egel, U. Lemmer, D. S. Wiersma, *Optica* **2018**, *5*, 1037; b) G. M. Conley, M. Burresi, F. Pratesi, K. Vynck, D. S. Wiersma, *Phys. Rev. Lett.* **2014**, *112*, 143901; c) G. Jacucci, J. Bertolotti, S. Vignolini, *Adv. Opt. Mater.* **2019**, *7*, 1900980; d) M. Leonetti, C. López, *Opt. Lett.* **2011**, *36*, 2824; e) L. Pattelli, G. Mazzamuto, D. S. Wiersma, C. Toninelli, *Phys. Rev. A* **2016**, *94*, 043846; f) E. Pini, G. Mazzamuto, F. Riboli, D. S. Wiersma, L. Pattelli, *Phys. Rev. Res.* **2024**, *6*, L032026.
[26] L. C. Andrews, R. L. Phillips, C. Y. Hopen, M. A. Al-Habash, *J. Opt. Soc. Am. A* **1999**, *16*, 1417.
[27] A. Brandstötter, A. Girschik, P. Ambichl, S. Rotter, *Proc. Natl. Acad. Sci. USA* **2019**, *116*, 13260.
[28] S. Aya, F. Araoka, *Nat. Commun.* **2020**, *11*, 3248.